$\mathbb{T}$-Operator Limits on Optical Communication: Metaoptics, Computation, and Input–Output Transformations

S. Molesky,[1,*] P. Chao,[1,*] J. Mohajan,[1] W. Reinhart,[2] H. Chi,[3] and A. W. Rodriguez[1]

[1] *Department of Electrical and Computer Engineering, Princeton University, Princeton, New Jersey 08544, USA*
[2] *Department of Materials Science and Engineering, Pennsylvania State University, University Park, Pennsylvania 16802, USA*
[3] *Siemens, Princeton, New Jersey 08540, USA*

We present an optimization framework based on Lagrange duality and the scattering $\mathbb{T}$ operator of electromagnetism to construct limits on the possible features that may be imparted to a collection of output fields from a collection of input fields, i.e., constraints on achievable optical transformations and the characteristics of structured materials as communication channels. Implications of these bounds on the performance of representative optical devices having multi-wavelength or multi-port functionalities are examined in the context of electromagnetic shielding, focusing, near-field resolution, and linear computing.

As undoubtedly surmised since long before Shannon's pioneering work on communication [1], or Kirchhoff's investigation of the laws governing thermal radiation [2], physics dictates that there are meaningful limits on how measurable quantities may be transferred between senders and receivers (collectively *registers*) that apply largely independent of the precise details by which transmission is realized. The noisy-coding theorem, for instance, proves that probabilistically error free message passing is not possible at any rate larger than the "channel capacity" [3]; while more recently, the possibility of utilizing entanglement as a novel resource has motivated the development of a variety of limits on communication in general quantum systems, e.g. Refs. [4–7]. Broadly, even at the coarsest levels of physical description, there is generally some notion of invariants, and the existence of such quantities implicitly precludes the possibility of realizing complete engineering control.

Equating registers with electromagnetic fields and scattering objects with channels [8], using the language of communication theory, it is thus reasonable to assume that there are certain channel-based limits on the extent that a collection of fields may be manipulated via material structuring. The wave nature of Maxwell's equations sets a fundamental relation between wavelength and frequency (for propagation) that cannot be arbitrarily altered by any realizable combination of material and geometry. Consequently, the scattered fields generated by any true object cannot be matched to any freely selected magnitude and phase profile, and so, certain transformations cannot be achieved with perfect fidelity (e.g. known limits on light trapping [9–11], cloaking bandwidths [12–14], delay-bandwidth products [15–17], etc.)

However, in establishing a means of evaluating the potential of present and future electromagnetic devices to address challenges requiring complex functionalities, such as artificial neural networks [18–21], spatial multiplexing [22–24] and computing [25–27], the important question is not whether such fundamental limitations exist, but rather what quantitative implications can be deduced in a given setting. Beyond well established considerations like the need to conserve power in passive systems and the classical diffraction limit of vacuum [28], such specific channel features are typically unknown [29]. Moreover, it is seldom clear what level of possible performance improvement could be sensibly supposed, even to within multiple orders of magnitude [30–32]. Archi-

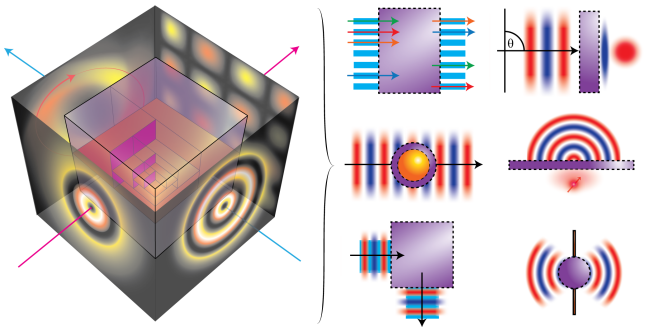

FIG. 1. **Investigation schematic and sample applications.** The figure sketches the central question explored in this article: given a specified design volume(s) and material(s), how effectively can some particular collection of field transformations (described as input–output pairs) be realized? The panel on the left depicts an abstract optical device, the imitable black-box, converting a known set of input electromagnetic field profiles into a desired set of output field profiles. The partitions interior to the design domain suggest how structural degrees of freedom or constraint clusters may be refined to improve design performance and estimations of limit performance (bounds), respectively. The smaller images to the right depict six (of the many) possible applications that can be easily described within this framework. Working from left-to-right, top-to-bottom, theses illustrations represent a spatial multiplexer, a metaoptic lens, a cloaking shell for an enclosed object, a light extractor (enhancing radiative emission from a dipolar source), a waveguide bend, and a directional antenna.

[*] Equal contribution

tectures possessing impressive field-transformation capabilities have already been demonstrated, from free-space (grating) couplers [33, 34] to beam steering [35, 36] and polarization control [37, 38], suggesting that large-scale optimization methods may allow scattering attributes to be tailored to a far greater degree than what has been seen in past intuition-based designs. Simultaneously, ramifying from the core ideas of Lagrange duality and interpreting physical relations as optimization constraints expounded below [39–42], a string of recent articles on improved bounds for scattering phenomena (including radiative heat transfer [32], absorbed power [43], scattered power [44], and Purcell enhancement [45]) have shown that, in some cases, only modest improvements over standard designs are even hypothetically attainable [44–53].

In this article, we demonstrate that this rapidly developing program for calculating bounds on scattering phenomena can be applied to determine limits on the accuracy to which any particular set of field transformations may be implemented, providing an initial exploration of channel characteristics in the context of classical electromagnetic (multi-wavelength and multi-port) devices. The article is broken into three sections. In Sec I, a condensed overview of related work examining channel limits on electromagnetic devices prior to the articles referenced above is provided. Section II then summarizes the guiding optimization outlook of the rest of the article along with current methods for constructing $\mathbb{T}$-operator (scattering theoretic) bounds. During this brief overview, two innovations necessary for handling generic input–output formulations are introduced: a further generalization on the variety of operator constraints that can be imposed based on the definition of the $\mathbb{T}$ operator, beyond the possibility of local clusters examined in Refs. [45, 51, 52], and a generalization of the type of vector image constraints that should be usually considered, as required to enforce that every transformation in an input–output set references the same underlying structure. Finally, Sec. III provides a number of exemplary applications of the theory, including studies of model computational kernels, domain shielding and near-field focusing. For the chosen loss function (the quadratic distance or two-norm between the set of desired target and realizable fields), the gap between calculated bounds and the performance of device geometries discovered via topology (or "density") optimization is regularly found to be of unit order. The observed trade-offs between the size of the design domain, the supposed material response of the device, the specific transformations (channels) considered, the number of constraint clusters, and the calculated limits reveal several intuitive trends. Most notably, achievable performance is strongly dependent on the nature and number of communication channels, with larger device sizes and indices of refraction resulting in greater achievable spatial resolution and transformations, in line with prior heuristics [REF]. For the wavelength-scale systems investigated here, the variability in achievable performance spans multiple orders of magnitude and, as demonstrated in Sec. III, tied to the ability of the formulation to enforce that all channel functionalities map to a unique (single) optimal geometry.

I. CHANNEL LIMITS IN PRIOR ART

Excluding techniques based on Lagrange duality to constrain electromagnetic design objectives, which are covered in greater detail in Sec. II, three major threads studied in prior art have substantially informed the findings and discussion below.

Decomposition—Any finite dimensional linear operator (or more generally any compact operator such as the scattering $\mathbb{T}$ operator of electromagnetism) has a corresponding singular value decomposition [54]. For almost any example of practical interest, particularly those with discrete representations, there are hence corresponding notions of rank and pseudo rank [8, 55–58].

Rank—Potential field transformations between collections of registers are inherently limited by any bounds on maximal rank or pseudo rank. Any set of channels connecting registers that do not overlap in space is inherently limited by the rank (pseudo rank) of its associated free propagation operators (the Green's function) [30, 44, 59, 60].

Size—The rank (pseudo rank) characteristics of free propagation in electromagnetics depend explicitly on geometry. That is, there are cases where possible field transformations are strongly limited by the spatial volume occupied by the registers [43, 59].

The main difference between past studies of channel limits utilizing these ideas and the $\mathbb{T}$-operator approach given in Sec. II lies in the incorporation of additional physical constraints concerning the generation of polarization currents (within a scattering object) in order to effect a desired transformation. More concretely, it is often possible to abstractly describe a device in terms of (possibly intersecting) design and observation regions. Taking a simplistic description of a near-field microscope as an example, the magnifying lens may be thought of as a design volume, and the final connection between the optical components and the electro–optic readout as an observation region. (As seen in Fig. 2, the design and observation regions are closely linked to the sender and receiver registers in optical communication.) Under this regional decomposition, the end goal of various applications can be understood as minimizing the power difference between the true total field created in the observation region ($\left|\mathbf{E}_o^t\right\rangle$) [42], resulting from a known incident field ($\left|\mathbf{E}^i\right\rangle$), and a given target output ($\left|\mathbf{E}_o^\diamond\right\rangle$):

$$\min_{\left|\mathbf{J}_d^g\right\rangle} \left\| \left|\mathbf{E}_o^t\right\rangle - \left|\mathbf{E}_o^\diamond\right\rangle \right\|_2^2. \tag{1}$$

(Here, subscripts mark domains of definitions and superscripts label different types of fields.) Supposing that polarizable media exists only within the design region (the device), following the notation of the upcoming section,

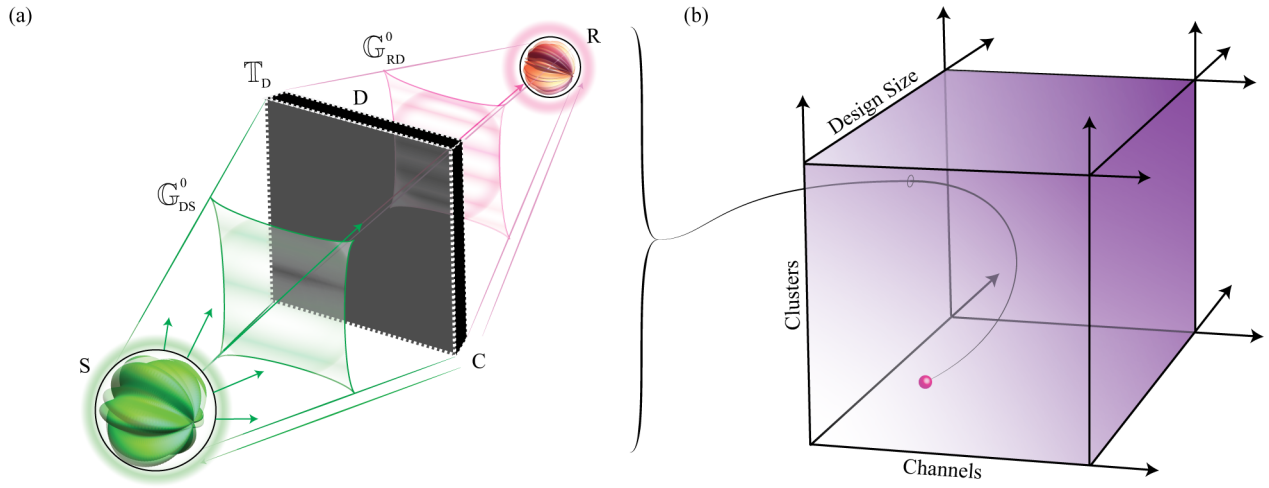

FIG. 2. **Electromagnetic channel limits.** (a) The properties of an electromagnetic channel(s) (**C**) depend on the environment connecting a particular (collection of) sender (**S**) and receiver (**R**) register(s), including characteristics like the volume each register occupies, their spatial separation, and the possibility of a transformation enabling polarizable device (**D**). Channel limits in prior art have been formulated predominately by analyzing the individual operators describing each of these aspects in isolation (e.g., the rank and pseudo rank of the free space Green's function between the sender and receiver volumes $\mathbb{G}^0_{\text{RS}}$). Here, in contrast, all environmental factors are treated simultaneously, accounting for the realities of interaction. (b) The difficulty of attaining device performance bounds using the formulation presented in Sec. II, for some predefined material, depends mainly on three variables: the number of regional constraints (spatial clusters) imposed, the number of channels (simultaneous transformations) considered, and the physical volume of the design region. The way in which these attributes determine how closely the computed bounds approximate achievable device performance is generally unknown and problem dependent. For radiative thermal emission and integrated absorption, increasing domain size leads to increasingly tight bounds when only a single constraint, the conservation of real power, is employed [43]. For radiative Purcell enhancement, recent results suggest that predictive bounds for larger design domains require a larger number of constraints [45]. Additional regional constraints, or concurrent analysis of additional channels, always produces tighter bounds.

in terms of the generated polarization field $\left|\mathbf{J}_d^g\right\rangle$ Eq. (1) becomes

$$\min_{\left|\mathbf{J}_d^g\right\rangle} \left\| \left|\mathbf{E}_o^i\right\rangle - \left|\mathbf{E}_o^\diamond\right\rangle + i\frac{Z}{k_o}\mathbb{G}_{od}^0\left|\mathbf{J}_d^g\right\rangle \right\|_2^2. \tag{2}$$

The minimum of Eq. (2) with respect to $\left|\mathbf{J}_d^g\right\rangle$,

$$i\frac{k_o}{Z}\left(\mathbb{G}_{od}^0\right)^\dagger\left(\left|\mathbf{E}_o^\diamond\right\rangle - \left|\mathbf{E}_o^i\right\rangle\right) = \left(\mathbb{G}_{od}^0\right)^\dagger \mathbb{G}_{od}\left|\mathbf{J}_d^g\right\rangle, \tag{3}$$

illustrates the necessity of the three notions stated above. First, even if Eq. (3) can be satisfied exactly, the minimum of Eq. (1) may be nonzero if the span of the target basis of $\mathbb{G}_{od}^0$ does not contain $\left|\mathbf{E}_o^\diamond\right\rangle - \left|\mathbf{E}_o^i\right\rangle$. Second, since in extending Eqs. (1)–(3) from single fields to collections nothing in the form of the minimum solution is altered, the rank (pseudo rank) of the Hermitian operator $\left(\mathbb{G}_{od}^0\right)^\dagger \mathbb{G}_{od}^0$ sets a limit on the number of channels that can connect (interact) with any register contained in the observation domain. Third, as highlighted by the explicit domain subscripts, the Green's function ($\mathbb{G}_{od}^0$) connecting the observation and design domains, on which the two previous points are based, depends on the geometric features of both regions.

While of obvious importance, it is clear that these observations do not fully encompass the difficulties associated with the larger question of realizing a given set of field transformations. Directly, without additional constraints, the challenge associated with attaining a particular polarization current $|\mathbf{J}_d^g\rangle$ within the design region cannot be inferred from Eq. (3). To include this information into the minimization of Eq. (1), additional physical constraints must be taken into account. Achieving this aim, without making the resulting problem statement computationally infeasible, is precisely the goal of the $\mathbb{T}$-operator framework presented below.

II. TECHNICAL DISCUSSION

A. Scattering theory, Lagrange duality, and limits

Following the sketch provided in Ref. [29] (supporting details can be found in Refs. [61–65]), there are two superficial distinctions that distinguish a scattering theory view of electromagnetics from Maxwell's equations. First, supposing a local, linear scattering potential, the fundamental wave relation from which all field properties are derived is

$$\mathbb{I}_s = \mathbb{I}_s\left(\mathbb{V}^{-1} - \mathbb{G}^0\right)\mathbb{T}_s, \tag{4}$$

where the s subscript denotes projection into the scattering object, $\mathbb{G}^0$ is the background Green's function of

the design domain Ω_s, throughout taken to be the vacuum Green's function (truncated to a problem-specific volume) scaled by $k_o^2 = (2\pi/\lambda)^2$ (so that all spatial dimensions may be simply defined relative to the wavelength), $\mathbb{V}$ is the bulk (spatially local) scattering potential of the material forming the design, $\mathbb{I}$ is the identity operator, and $\mathbb{T}_s$ is the scattering operator, formally defined by Eq.(4) [66] [67]. (Although more general descriptions are possible, it is implicitly assumed throughout this article that $\mathbb{V} = \mathbb{I}\chi$, where χ is electric susceptibility of some isotropic medium.) Second, one of either the electromagnetic field or polarization field is singled out as an initial [68], and all other fields are generated via the scattering operator $\mathbb{T}_s$. This leads to a division of the theory into two classes: initial flux problems, where a far-field incident flux $\big|\mathbf{E}^i\big\rangle$ is assumed, generating a polarization current $|\mathbf{J}^g\rangle = -\left(ik_o/Z\right)\mathbb{T}_s\big|\mathbf{E}^i\big\rangle$ and scattered field $\big|\mathbf{E}^s\big\rangle = \left(iZ/k_o\right)\mathbb{G}^0\big|\mathbf{J}^g\big\rangle$, and initial source problems, where a polarization source $\big|\mathbf{J}^i\big\rangle$ is assumed, generating an electromagnetic field $|\mathbf{E}^g\rangle = \left(iZ/k_o\right)\mathbb{G}^0\mathbb{T}_s\mathbb{V}^{-1}\big|\mathbf{J}^i\big\rangle$ and total current $\big|\mathbf{J}^t\big\rangle = \mathbb{T}_s\mathbb{V}^{-1}\big|\mathbf{J}^i\big\rangle$.

Given that most quantities related to power transfer result from inner products between electromagnetic and polarization fields [61], many common design objectives within scattering theory, encompassing applications varying from enhancing the amount of radiation that can be extracted from a quantum emitter [69–71] to increasing absorption into a photovoltaic cell [72–74], are given by sesquilinear forms on the scattering operator $\mathbb{T}_s$. As the central example investigated in this article, continuing the discussion of Sec. I and covering all the specific applications treated in Sec. III, suppose that a collection of fluxes $\left\{\big|\mathbf{E}_k^i\big\rangle\right\}$, with k ranging over some finite indexing set, is incident on a scattering design region Ω. Assume that the goal of the (input–output) device is to create a set $\left\{\big|\mathbf{E}_k^\diamond\big\rangle\right\}$ of target fields within an observation region Ω_o, marked by a domain subscript o and spatial projection operator $\mathbb{I}_o$, i.e. a collection of register mappings $\big|\mathbf{E}_k^i\big\rangle \mapsto \big|\mathbf{E}_k^\diamond\big\rangle$. Taking the Euclidean norm as a metric of design performance,

$$\operatorname{dist}\left(\left\{\big|\mathbf{E}_k^t\big\rangle\right\},\left\{\big|\mathbf{E}_k^\diamond\big\rangle\right\}\right) = \sqrt{\sum_k \left\|\mathbb{I}_o\left(\big|\mathbf{E}_k^t\big\rangle - \big|\mathbf{E}_k^\diamond\big\rangle\right)\right\|_2^2}, \tag{5}$$

the equivalent objective (in the sense (5) and (6) have the same minimum)

$$\operatorname{Obj}\left(\left\{\big|\mathbf{E}_k^t\big\rangle\right\},\left\{\big|\mathbf{E}_k^\diamond\big\rangle\right\}\right) = \sum_k \left\|\mathbb{I}_o\left(\big|\mathbf{E}_k^t\big\rangle - \big|\mathbf{E}_k^\diamond\big\rangle\right)\right\|_2^2 \tag{6}$$

is effectively a sesquilinear form on $\mathbb{T}_s$.

$$\begin{aligned}\operatorname{Obj} &= \sum_k \big\langle \mathbf{E}_k^\diamond\big|\mathbb{I}_o\big|\mathbf{E}_k^\diamond\big\rangle - 2\operatorname{Re}\left[\big\langle \mathbf{E}_k^\diamond\big|\mathbb{I}_o\big|\mathbf{E}_k^t\big\rangle\right] + \big\langle \mathbf{E}_k^t\big|\mathbb{I}_o\big|\mathbf{E}_k^t\big\rangle \\ &= \sum_k \big\langle \mathbf{E}_k^\diamond\big|\mathbb{I}_o\big|\mathbf{E}_k^\diamond\big\rangle - 2\operatorname{Re}\left[\big\langle \mathbf{E}_k^\diamond\big|\mathbb{I}_o\big|\mathbf{E}_k^i\big\rangle\right] + \big\langle \mathbf{E}_k^i\big|\mathbb{I}_o\big|\mathbf{E}_k^i\big\rangle \\ &\quad + \big\langle \mathbf{E}_k^i\big|\mathbb{T}_s^\dagger\mathbb{G}^{0\dagger}\mathbb{I}_o\mathbb{G}^0\mathbb{T}_s + 2\operatorname{Sym}\left[\mathbb{I}_o\mathbb{G}^0\mathbb{T}_s\right]\big|\mathbf{E}_k^i\big\rangle \\ &\quad - 2\operatorname{Re}\left[\big\langle \mathbf{E}_k^\diamond\big|\mathbb{I}_o\mathbb{G}^0\mathbb{T}_s\big|\mathbf{E}_k^i\big\rangle\right],\end{aligned} \tag{7}$$

and the objective of the design amounts to a minimization of

$$\begin{aligned}\operatorname{Obj}\left(\mathbb{T}_s\right) = \sum_k &\big\langle \mathbf{E}_k^i\big|\mathbb{T}_s^\dagger\mathbb{G}^{0\dagger}\mathbb{I}_o\mathbb{G}^0\mathbb{T}_s + 2\operatorname{Sym}\left[\mathbb{I}_o\mathbb{G}^0\mathbb{T}_s\right]\big|\mathbf{E}_k^i\big\rangle \\ &- 2\operatorname{Re}\left[\big\langle \mathbf{E}_k^\diamond\big|\mathbb{I}_o\mathbb{G}^0\mathbb{T}_s\big|\mathbf{E}_k^i\big\rangle\right].\end{aligned} \tag{8}$$

Here, $\operatorname{Sym}\left[\mathbb{O}\right]$ and $\operatorname{Asym}\left[\mathbb{O}\right]$ denote symmetric (Hermitian) and anti-symmetric (skew-hermitian) parts of $\mathbb{O}$. (Other objective forms, e.g. originating from other norms, could also be considered, but (8) offers many useful simplifications for both analysis and computation.) Acting with $\mathbb{T}_s^\dagger$ from the left on (4), giving $\mathbb{T}_s^\dagger = \mathbb{T}_s^\dagger\mathbb{U}^\dagger\mathbb{T}_s$ with $\mathbb{U}^\dagger = \mathbb{V}^{-1} - \mathbb{G}^0$ so that $\operatorname{Asym}\left[\mathbb{U}\right]$ is positive definite, shows that the physical constraints of scattering theory can also be written as similar sesquilinear forms. As such, any electromagnetic design objective of this input–output form (Ref. [42]) can be cast as a quadratically constrained quadratic program [75, 76] (QCQP) by treating $\mathbb{T}_s$ as a vector, i.e.

$$\begin{aligned}&\min{}_{\mathbb{T}_s}\ \operatorname{Obj}\left(\mathbb{T}_s\right) \\ &\text{such that } (\forall\, l,m)\ \big\langle \mathbf{B}_l\big|\mathbb{T}_s\big|\mathbf{B}_m\big\rangle = \big\langle \mathbf{B}_l\big|\mathbb{T}_s^\dagger\mathbb{U}\mathbb{T}_s\big|\mathbf{B}_m\big\rangle,\end{aligned} \tag{9}$$

over some basis [77] for the space of electromagnetic fields over the design region Ω_s. Although QCQP problems are part of the non-deterministic polynomial-time (NP) hard complexity class, a number of relaxation techniques, as well as a range of well developed solvers, are known to often yield accurate solution approximations [78] (that may in fact be exact). Principally, letting $\mathcal{L}\left(\mathbb{T}_s,\boldsymbol{\lambda}\right) = \operatorname{Obj}\left(\mathbb{T}_s\right) + \boldsymbol{\lambda}\,\boldsymbol{\mathcal{C}}\left(\mathbb{T}_s\right)$ be the Lagrangian of Eq. (9), with $\boldsymbol{\mathcal{C}}\left(\mathbb{T}\right)$ denoting the collection of imposed scattering constraints and $\boldsymbol{\lambda}$ the associated set of Lagrange multipliers, it always possible to relax Eq. (9), or any differentiable optimization problem for that matter [79], to a convex problem by considering the unconstrained dual optimization problem

$$\max{}_{\boldsymbol{\lambda}}\ \mathcal{G}\left(\boldsymbol{\lambda}\right), \tag{10}$$

with $\mathcal{G}\left(\boldsymbol{\lambda}\right) = \min_{\mathbb{T}_s}\ \mathcal{L}\left(\mathbb{T}_s,\boldsymbol{\lambda}\right)$. Because any true solution of Eq. (9) requires every constraint relation to be satisfied, for any collection of multipliers $\boldsymbol{\lambda}$, $\mathcal{G}\left(\boldsymbol{\lambda}\right)$ is always smaller (resp. larger if the optimization objective is to maximize some quantity) than any solution of the primal (original) optimization. Thus, in addition to providing a means of obtaining approximate solutions to Eq. (9) [78],

solving Eq. (10) also determines a bound, or limit, on the performance that could be possibly achieved by any realizable device geometry. By varying the constraints included in (9) these bounds can be tailored to encompass select attributes of the channel(s) as one wishes, such as qualifications on material composition (via $\mathbb{V}$), the available design domain (via truncation of $\mathbb{G}^0$), and the actual input fields (via $\left\{\left|\mathbf{E}_k^i\right\rangle\right\}$). Further, although we have not seriously examined the prospect, it is also possible to apply similar reasoning to objective forms differing substantially from Eq. (6).

B. Mean-field hierarchy (spatially localized constraints)

Building on the above perspective, as described in greater detail in Refs. [45, 53], the $\mathbb{T}$ operator provides a natural means of obtaining arbitrarily accurate, context specific, mean-field solution approximations. The operator relation given by Eq. (4) is equally valid under evaluation with any linear functional or vector, or composition with any other maps, and can hence be "coarse-grained" (averaged). Expressly, to construct an appropriate mean-field approximation, take $\mathbb{P}_{\Omega_c}$ to denote a generalized spatial projection operator into the spatial cluster (subregion) Ω_c, with the added freedom that, at any point within Ω_c, $\mathbb{P}_{\Omega_c}$ may transform the field in any way. That is, taking the three dimensional nature of the electromagnetic and polarization vector fields into account, $\mathbb{P}_{\Omega_c}$ may be any operator of the form

$$\mathbb{P}_{\Omega_c}(\mathbf{x},\mathbf{y}) = \begin{cases} \overline{\mathbf{0}} & \mathbf{x} \neq \mathbf{y} \text{ or } \mathbf{x} \notin \Omega_c \\ \overline{\mathbf{M}}_{\mathbf{x}} & \mathbf{x} = \mathbf{y} \text{ and } \mathbf{x} \in \Omega_c \end{cases}, \tag{11}$$

where $\overline{\mathbf{M}}_{\mathbf{x}}$, at any point in Ω_c, is some any linear operator (3×3 matrix) on the three-dimensional vector space at the point $\mathbf{x}$. Recalling that $\mathbb{I}_s$ is defined as

$$\mathbb{I}_s(\mathbf{x},\mathbf{y}) = \begin{cases} \overline{\mathbf{0}} & \mathbf{x} \neq \mathbf{y} \text{ or } \mathbf{x} \notin \Omega_s \\ \overline{\mathbf{1}} & \mathbf{x} = \mathbf{y} \text{ and } \mathbf{x} \in \Omega_s \end{cases}, \tag{12}$$

with $\overline{\mathbf{1}}$ the identity operator (3×3 identity matrix), and that the composition of any two spatial projections is equivalent to a single spatial projection into the intersection of the two regions, any operator of the form given by Eq. (11) commutes with $\mathbb{I}_s$, regardless of the actual geometry of the scatterer, allowing Eq. (4) to be rewritten as

$$\begin{aligned} &\mathbb{T}_s^\dagger \mathbb{P}_{\Omega_c}^\dagger \mathbb{I}_s = \mathbb{T}_s^\dagger \mathbb{P}_{\Omega_c}^\dagger \mathbb{I}_s \left(\mathbb{V}^{-1} - \mathbb{G}^0\right) \mathbb{T}_s \\ &\Rightarrow \mathbb{T}_s^\dagger \mathbb{I}_s \mathbb{P}_{\Omega_c}^\dagger = \mathbb{T}_s^\dagger \mathbb{P}_{\Omega_c}^\dagger \mathbb{I}_s \left(\mathbb{V}^{-1} - \mathbb{G}^0\right) \mathbb{T}_s \\ &\Rightarrow \mathbb{T}_s^\dagger \mathbb{P}_{\Omega_c}^\dagger = \mathbb{T}_s^\dagger \mathbb{P}_{\Omega_c}^\dagger \left(\mathbb{V}^{-1} - \mathbb{G}^0\right) \mathbb{T}_s \\ &\Rightarrow \mathbb{P}_{\Omega_c} \mathbb{T}_s = \mathbb{T}_s^\dagger \mathbb{U} \mathbb{P}_{\Omega_c} \mathbb{T}_s. \end{aligned} \tag{13}$$

Working with increasingly refined collections of clusters, sets of subdomains $\{\Omega_c\}$ with c ranging over some indexing set such that $\cup_c \Omega_c = \Omega$, Eq. (13) leads to increasingly refined mean-field approximations that mirrors the "bottom up" optimization of a given objective with respect to structural degrees of freedom [80]. Letting $|\mathbf{E}\rangle$ denote some predefined electromagnetic flux, and making the simplifying choice that $\overline{\mathbf{M}}_{\mathbf{x}} = \overline{\mathbf{1}}$ for all $\mathbf{x} \in \Omega_c$ acting on Eq. (13) with $\langle\mathbf{E}| \ldots |\mathbf{E}\rangle$ gives

$$\begin{aligned} &\int_{\Omega_c} d\mathbf{x} \left[\mathbf{E}^*(\mathbf{x}) \cdot \mathbf{T}(\mathbf{x}) - \int_{\Omega} d\mathbf{y}\ \mathbf{T}^*(\mathbf{y}) \cdot \overline{\mathbf{U}}(\mathbf{y},\mathbf{x}) \cdot \mathbf{T}(\mathbf{x}) \right] \\ &= \langle\mathbf{E}|\mathbb{P}_{\Omega_c}|\mathbf{T}\rangle - \langle\mathbf{T}|\mathbb{U}\mathbb{P}_{\Omega_c}|\mathbf{T}\rangle = 0, \end{aligned} \tag{14}$$

where the generated polarization current $|\mathbf{T}\rangle$ is the image of $|\mathbf{E}\rangle$ under the action of $\mathbb{T}_s$ ($\mathbb{T}_s|\mathbf{E}\rangle \mapsto |\mathbf{T}\rangle$). Returning to Eq. (14), the selection of any cluster Ω_c therefore defines an averaging kernel for the scattering theory: over Ω_c the otherwise free field must respect the true physical equations of electromagnetism, however, at any point $\mathbf{x} \in \Omega_c$ unphysical fluctuations of the field (deviations of the integrand from zero) are permitted [81].

As any physical polarization current field $|\mathbf{J}^g\rangle$ will automatically satisfy any relation of the form of Eq. (14), any optimization that only imposes such relations over a finite set of clusters $\{\mathbb{P}_k\}$ will automatically possess objective values at least as optimal as what can be achieved if Eq. (4) is imposed in full. Hence, solving the mean-field optimization

$$\begin{aligned} &\min \text{ / } \max {}_{|\mathbf{T}\rangle}\ \mathrm{Obj}\left(|\mathbf{T}\rangle\right) \\ &\text{such that } (\forall\ \Omega_k)\ \langle\mathbf{E}|\mathbb{P}_{\Omega_k}|\mathbf{T}\rangle - \langle\mathbf{T}|\mathbb{U}\mathbb{P}_{\Omega_k}|\mathbf{T}\rangle, \end{aligned} \tag{15}$$

similar to the mean-field theories used in statistical physics [82, 83], game theory [84, 85] and machine-learning [86, 87], results in a bound (limit) on physically realizable performance [88]. Due to the implicit wavelength scale contained in the Green's function ($\mathbb{G}^0$ in $\mathbb{U}$), there is, for most objectives, no meaningful difference between a mean-field fluctuating sufficiently rapidly and a physical field, satisfying Eq. (4) exactly. As a consequence, smaller clusters, effectively, lead to higher order mean-field theories that more closely bound what is actually possible. This tightening with decreasing cluster size causes (15) to act as an intriguing complement to standard structural design. In "bottom-up" geometric optimization, the introduction of additional degrees of freedom opens additional possibilities that improve achievable optima. In "top-down" mean-field optimization, the introduction of additional clusters results in additional constraints that reduce the space of possibilities available to the design field $|\mathbf{T}\rangle$. Our present high-level approach to solving Eq. (15) is described in Ref. [45].

C. Multiple transformations (channels)

When handling a collection of sources that span a relatively small subspace, an efficient approach to computing $\mathbb{T}$ operator bounds through Eqs. 8 & 13 is to work

with individual inputs and outputs. Take $\{|\mathbf{S}_k\rangle\}$ to be a given collection of sources, and let $\{|\mathbf{T}_k\rangle\}$ be the collection of polarization fields resulting from the action of $\mathbb{T}_s$, $\mathbb{T}_s\,|\mathbf{S}_k\rangle \mapsto |\mathbf{T}_k\rangle$. Following Ref. [45], for any pair of indices $\langle k_1, k_2\rangle$, and each $\mathbb{P}_{\Omega_c}$ cluster operator, $|\mathbf{S}_{k_1}\rangle$ and $\{|\mathbf{T}_{k_1}\rangle, |\mathbf{T}_{k_2}\rangle\}$ must obey the relation

$$\langle \mathbf{S}_{k_1}|\,\mathbb{P}_{\Omega_c}\,|\mathbf{T}_{k_2}\rangle = \langle \mathbf{T}_{k_1}|\,\mathbb{U}\mathbb{P}_{\Omega_c}\,|\mathbf{T}_{k_2}\rangle\,, \tag{16}$$

where, again, $\mathbb{U} = \mathbb{V}^{-1\dagger} - \mathbb{G}^{0\dagger}$, and $\langle \mathbf{F}|\mathbf{G}\rangle$ denotes the standard complex-conjugate inner product over the complete domain ($\langle \mathbf{F}|\mathbf{G}\rangle = \int_\Omega d\mathbf{x}\; \mathbf{F}\,(\mathbf{x})^* \cdot \mathbf{G}\,(\mathbf{x})$ in the spatial basis). In Eq.(16), the extension to pairs of sources and polarization fields, compared to the single source constraints examined in Ref. [45], is necessary to account for the fact that a single scattering object (structured media) simultaneously generates each $|\mathbf{T}_k\rangle$ from each $|\mathbf{S}_k\rangle$. Over some set of clusters, using only the "diagonal" constraint between each source field ($|\mathbf{S}_k\rangle$) and polarization response ($|\mathbf{T}_k\rangle$) is equivalent to considering each source independently. But, by additionally including "off-diagonal" interactions between pairs, Eq. (16) introduces the requirement of a single consistently defined scattering object. Supposing a spatial basis in the limit of "point" (vanishingly small) clusters and complete field mixing, Eq. (16) becomes ($\forall\; x \in \Omega\;\&\;\langle k_1, k_2\rangle$)

$$\begin{aligned}&\mathbf{S}^*_{k_1}\,(\mathbf{x}) \cdot \overline{\mathbf{M}}_{\mathbf{x}} \cdot \mathbf{T}_{k_2}\,(\mathbf{x}) \\ &= \left(\int_\Omega d\mathbf{y}\; \mathbf{T}^*_{k_1}\,(\mathbf{y}) \cdot \overline{\mathbf{U}}\,(\mathbf{y},\mathbf{x})\right) \cdot \overline{\mathbf{M}}_{\mathbf{x}} \cdot \mathbf{T}_{k_2}\,(\mathbf{x})\,.\end{aligned} \tag{17}$$

Therefore, making use of the possible freedom in the definition of $\overline{\mathbf{M}}_{\mathbf{x}}$, whenever any $\mathbf{T}_{k_n}\,(\mathbf{x})$ is nonzero any of the three local vector coordinates we must have

$$\mathbf{S}^*_k\,(\mathbf{x}) = \int_{\Omega_s} d\mathbf{y}\; \mathbf{T}^*_k\,(\mathbf{y}) \cdot \overline{\mathbf{U}}\,(\mathbf{y},\mathbf{x})\,, \tag{18}$$

for all k and $\mathbf{x} \in \Omega_s$, the collection of all spatial points in Ω where some $\mathbf{T}_k\,(\mathbf{x}) \neq \mathbf{0}$. Taking the adjoint, the totality of the point constraints given by Eq. (18) can be codified as

$$|\mathbf{T}_k\rangle = \left(\mathbb{U}^\dagger_{\Omega_s}\right)^{-1} |\mathbf{S}_k\rangle\,. \tag{19}$$

Comparing with Eq. (4), Ω_s thus determines the unique geometry of the scattering object (structured medium) for all sources.

III. APPLICATIONS

In this section, the ideas presented in Sec. II are applied to several example applications, expounding the use of input–output language to describe physical design as QCQP optimization problems, and demonstrating the utility and tightness of the associated bounds. Three main overarching features, which credibly apply beyond the actual scope studied, are seen. First, distinct channels can display widely varying (often unintuitive) characteristics. Second, both in terms of computed bounds and the findings of inverse design, attainable performance may vary greatly as the number of channels increases—the design freedom offered by spatial structuring in a wavelength scale device is by no means inexhaustible. Third, increasing the number of constraint clusters can improve the accuracy of bounds calculations, but this improvement is problem dependent and varies, in particular, with the material assumed. Throughout, as no feature size can be imposed if one wishes to set bounds on any possible geometry, quoted inverse design values represent the performance of "grayscale" structures, allowing each pixel to take on any susceptibility value of the form $t\chi$ with $t \in [0, 1]$.

A. Field screening

Objective—Minimize the spatially integrated field intensity over a subwavelength ball for two dipole fields, supposing that the distribution of scattering material (of a predefined susceptibility) must be contained in a thin surrounding shell.

The observation (shielded) region is taken to have a radius of 0.2 λ, while the design domain is confined within a shell of inner radius 0.2 λ and outer radius 0.24 λ. As sketched in the inset of Fig. 3(a), the "separation vectors" connecting the center of each dipole sources to the center of the observation domain are supposed to be aligned. The loss objective is defined as

$$\mathrm{Loss}\left(\left|\mathbf{E}^t_a\right\rangle, \left|\mathbf{E}^t_b\right\rangle\right) = \frac{\|\mathbb{I}_{\mathrm{obs}}\left|\mathbf{E}^t_a\right\rangle\|_2^2 + \|\mathbb{I}_{\mathrm{obs}}\left|\mathbf{E}^t_b\right\rangle\|_2^2}{\|\mathbb{I}_{\mathrm{obs}}\left|\mathbf{E}^i_a\right\rangle\|_2^2 + \|\mathbb{I}_{\mathrm{obs}}\left|\mathbf{E}^i_b\right\rangle\|_2^2} \tag{20}$$

with $\|\ldots\|_2$ denoting the Euclidean two-norm and $\mathbb{I}_{\mathrm{obs}}$ projection into the observation domain. Two clusters, evenly dividing the radius of the design region ($0.2 \to 0.22$ λ and $0.22 \to 0.24$ λ), are used in all bound computations.

In the limit of large separation, the dipole fields within the design and observation domains closely resemble counter-propagating planewaves. Hence, the constant asymptote value seen as d approaches λ is, for all practical purposes, a bound on shielding for two opposing planewaves. The decrease of the bounds for small separation, speculatively, is caused by a combination of localization effects. As the dipoles are brought into the near-field of the design, the bulk of the field magnitude increasingly shifts towards the edge of the observation region. Consequently, inducing small shifts in the position of the field results in a comparatively larger field expulsion. The presence of relatively larger evanescent fields likely also simplifies the suppression of total emission via the (inverse) Purcell effect.

The imposition of cross-constraints (solid lines), which in the limit of point clusters enforce that all considered

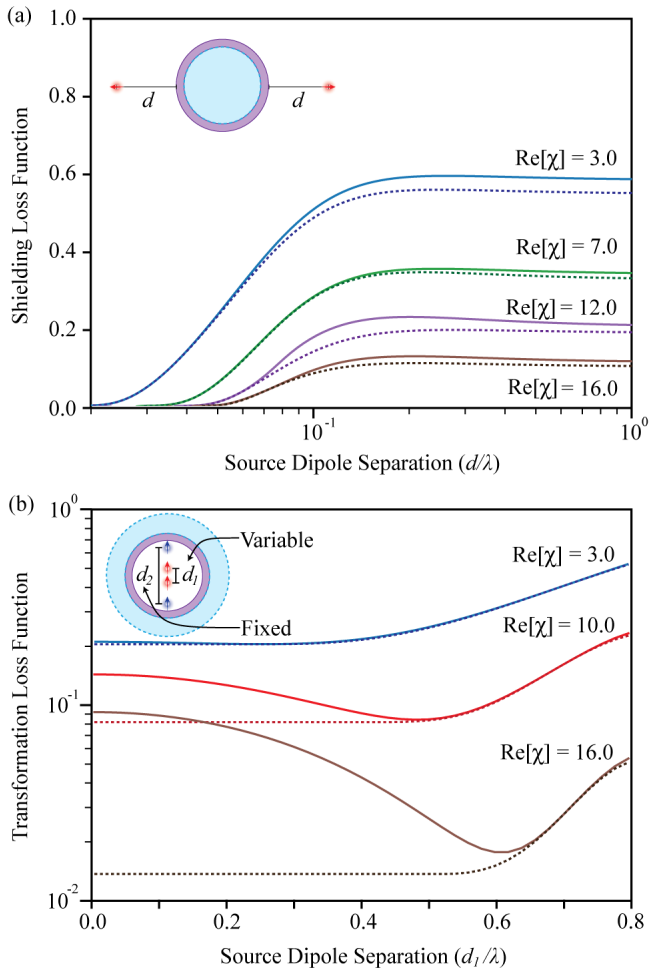

FIG. 3. **Dipole screening and field transformations.** The figure depicts two representative three-dimensional applications of input–output bounds: limits on the ability of any structured geometry confined to a thin shell to (a) screen dipole fields, and (b) mask the separation of dipole source pairs within the encompassing environment. In both situations, dashed lines mark independent bounds, calculated without the inclusion of cross-constraints which enforce a unique optimal structure across all field transformations, while the solid lines result when source interactions effects are taken into account. A material loss value of $\mathrm{Im}\,[\chi] = 0.01$ is assumed for all cases.

channels are realized within one common geometry (see Sec. II C), is seen to produce a relatively small correction to the bounds attained for independently optimized channels (dashed lines). This suggests that although perfect shielding is not possible at sufficiently large dipole separation, given the small shell and material constraints investigated, many structures may potentially achieve similar performance, i.e. the considered channels have yet to "set" the scattering structure in any meaningful way.

B. Dipole resolution and masking

Objective—Manipulate the field emanating from a pair of axially aligned dipoles, again limiting the volume available for device design to a thin encompassing spherical shell, so that exterior to the shell it appears that the dipoles are separated by either a larger or smaller distance. If the field is altered so that the separation distance appears larger than it actually is, it is easier to resolve that there are in fact two dipoles present, instead of a single dipole of some effective strength.

More exactly, the input field is generated by a pair of $\mathbf{z}$ polarized dipole sources, labeled 1 and 2, situated at $+d_i\hat{\mathbf{z}}$ and $-d_i\hat{\mathbf{z}}$ for $i = 1, 2$, and the target field is taken to arise from equivalent dipolar configuration with a distinct separation, $\pm d_t\hat{\mathbf{z}}$. The observation domain is set to be a shell of half wavelength thickness enveloping the design domain, which extends from an inner radius of 0.48 λ to an outer radius of 0.5 λ. Bounds, in all cases, are computed using ten spherical clusters, evenly spanning the design domain with respect to radius. Additional technical details concerning the example are given in Sec. V A.

The bounds depicted in the three heat maps of Fig. 4, exploring variations in both input $d_1 = d_2$ and output d_t pair separations, indicate that the challenge of either reducing or enlarging the perceived separation of the source varies sizably with supposed material properties and gap distances. For larger target or source separations (dipoles approaching the interior surface of the design domain) the increasingly dominant role of evanescent fields makes almost any transformation challenging, especially in weakly polarizable media. Focusing on Fig. 4(b), where the real part of the permittivity is limited to small positive numbers (weak dielectrics), the bounds prove that neither separation manipulation behavior is achievable in any practical sense when the input and target separations vary by more than ≈ 0.25 λ. Conversely, even under the imposition of considerably larger material loss ($\mathrm{Im}\,[\chi]$), panel (a) suggests that much better performance is achievable with metals ($\mathrm{Re}\,[\chi] < -1$). Intuitively, the subwavelength characteristics of the system do not preclude resonant response in this case since plasmon excitations remain possible. The observed asymmetry between increasing and reducing perceived separation seen in panels (b) and (c), which is largely absent in the metallic example of panel (a), is likely also tied to decaying waves: larger gaps produce larger evanescent fields in the observation domain compared to what is provided by the source, but smaller target separations do not.

Figure 3(b) explores the impact of distinct source separations, varying d_1 while keeping $d_2 = 0.7$ λ fixed, for a common target field corresponding to two co-located dipoles at the center of the ball, $d_t = 0$. The findings highlight the need to enforce that performance bounds for multiple channels refer to a unique scattering geometry, achieved via the presence of cross-constraints in the optimization (see Sec. II C). When the two channels are analyzed separately (dashed lines), the bound values match

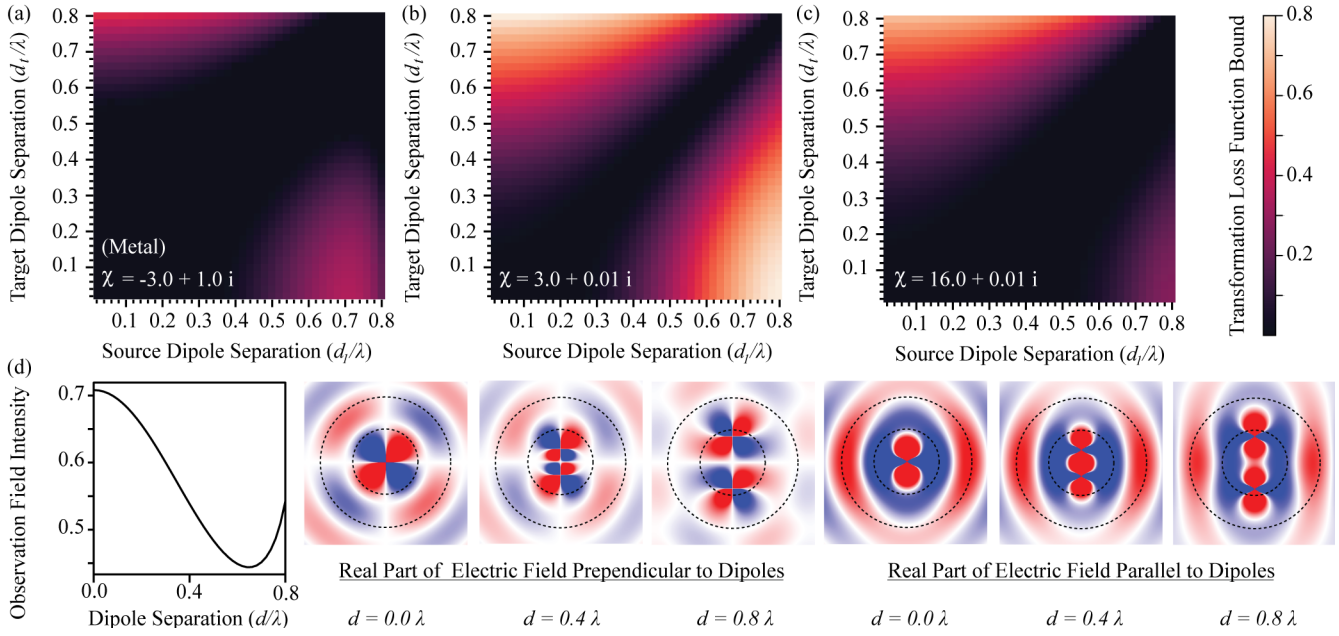

FIG. 4. **Dipole resolution and masking.** Considering the same three-dimensional system depicted in the inset of Fig. 3(b), but with a single dipole-pair source, the three heat maps depict bounds on the ability of an arbitrary geometry made from a specified material, restricted to a thin shell, to modify the perceived separation of a pair of axially aligned dipole sources, as implied by the electric field exterior to the design. Setup details are given in the main text. In moving from the trivial diagonal (no transformation) to the top left, the target field is set to be the field of an axial dipole pair further separated than that of the source. Opposingly, in moving to the bottom right, the target field is set to be the field of an axial dipole pair less separated than that of the source. The observed asymmetry between these two directions provides evidence of the ostensibly greater challenge of resolving closely separated fields, compared to masking separation. Field profiles for representative dipole pairs, along with the average field intensity within the observation domain (dashed lines), are given in panel (d).

those displayed on the heat maps of Fig. 4, with the contribution of source 1 to the loss function approaching zero as $d_1 \to 0$, since in this regime the source and target fields match. However, when cross-constraints are included, the lack of a need for a design in this regime for the first source is at odds with what is needed to convert the field of the widely separated d_2 source, leading to degraded performance. As d_1 approaches d_2, the requirement of a unique gemometry no longer introduces additional requirements, and thus the "simultaneous" (cross-constrained) and "independent" results merge.

C. Math kernels (integration and differentiation)

Objective—Within a bounding rectangle, design a two-dimensional scattering profile, for a known collection of incident waves, such that the relation between each incident field and total field, along specified input and output observation planes, reproduces the action of Volterra (integration) or differentiation operator. Given that the Volterra and differentiation kernels are two of the basic elements of differential equations, these examples are of considerable interest in relation to recent proposals for optical computing [25–27].

The design region is chosen to have a transverse length (thickness) of 0.5 λ and parallel length of 2 λ, insets Fig. 5(a) and Fig. 5(c). The input observation plane is set at distance of 0.25 λ from the input edge of the design region, and the output observation plane is located at a distance of 0.25 λ from the output edge of the design region. Incident fields are generated by dipole (pixel) sources placed on a source plane, running parallel to the long edge of the design region, situated at a distance 0.2 λ from the input observation plane. The source plane has length of 1.5 λ and is centered in relation to the design domain, creating a 0.25 λ offset from the top and bottom edges of the design region and input and output planes. For the Volterra operator, the target fields along the output plane, letting y denote the direction running parallel to the long edge of the design region, are calculated as $\mathbf{E}^{\diamond}(x_{\diamond}, y) = \int_0^y \mathrm{d}y'\ \mathbf{E}^{i}(x_i, y')$, with $x_{\diamond}$ and x_i denoting the common coordinate of the output and input plane, respectively. For the differential operator, keeping the above notation, the target fields are calculated as $\mathbf{E}^{\diamond}(x_{\diamond}, y) = \partial \mathbf{E}^{i}(x_i, y)/\partial y$, implemented as a finite-difference approximation on a computational grid. The optimization objective is defined by Eq. (7) and the bounds formulated following the description given in Sec. II. Further implementation details appear in Sec. V B. The loss function values appearing in

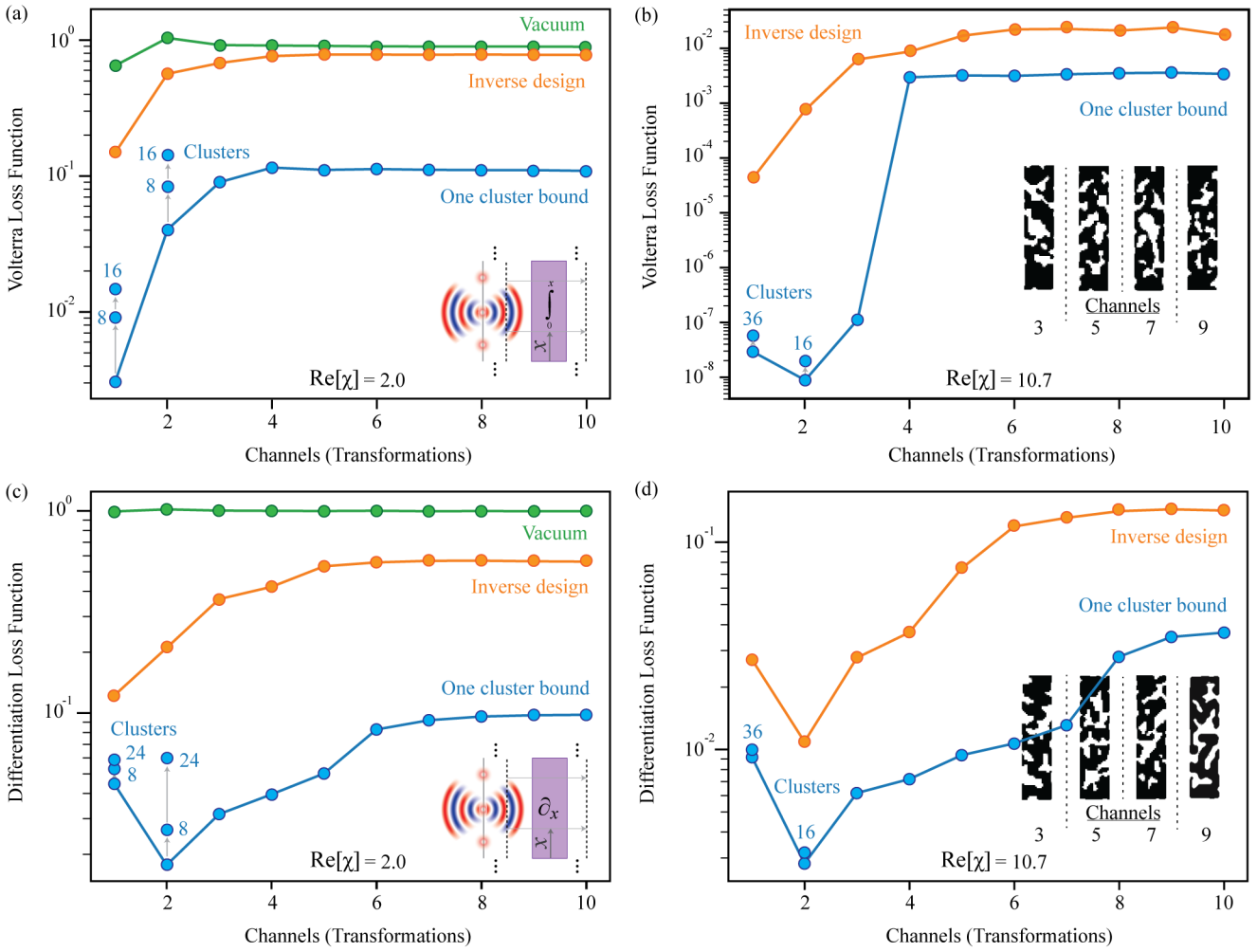

FIG. 5. **Volterra and differentiation kernels.** Following the description in the main text, the figure depicts limits on the degree to which a structured medium of a given electric susceptibility χ, confined to a rectangular design domain, may implement Volterra (top row) and differentiation (bottom row) kernels, as as function of the size of the subbasis (number of channels or transformations) over which the operator is defined. The cluster labels reference the number of cluster constraints imposed on the design domain, following the discussion of Sec. II and with further details given in the main text. Notably, the calculated bounds generally agree to within an order of magnitude of the performance of inverse designed structures when either the rank of the specified subbasis, or number of imposed clusters, is large. In all four cases, a material loss value of $\mathrm{Im}\,[\chi] = 0.01$ is assumed. Representative topology-optimized structures are included as insets in (b) and (d). The performance of these binarized systems is roughly a factor of two worse than the associated "grayscale" geometries compared to in the figure.

Fig. 5 are determined by

$$\mathrm{Loss}\left(\left|\overline{\mathbf{E}^t}\right\rangle\right) = \frac{\|\mathbb{I}_{\mathrm{out}}\left(\left|\overline{\mathbf{E}^t}\right\rangle - \left|\overline{\mathbf{E}^\diamond}\right\rangle\right)\|_2^2}{\|\mathbb{I}_{\mathrm{out}}\left|\overline{\mathbf{E}^i}\right\rangle\|_2^2 + \|\mathbb{I}_{\mathrm{out}}\left|\overline{\mathbf{E}^\diamond}\right\rangle\|_2^2}. \tag{21}$$

In Eq. (21), $\mathbb{I}_{\mathrm{out}}$ denotes projection onto the output observation plane, and an overline on a vector indicates vertical concatenation over all like named fields indexed by the incident waves, i.e. $\left|\overline{\mathbf{E}^t}\right\rangle = \left[\left|\mathbf{E}_1^t\right\rangle, \ldots, \left|\mathbf{E}_N^t\right\rangle\right]$ for N sources. The cluster numbers appearing in Fig. 5 refer to specific, even and consistent, divisions of the design domain rectangle along its long and short edges. Writing division of the short edge first, $8 = 2 \times 4$, $16 = 2 \times 8$, $24 = 3 \times 8$ and $36 = 3 \times 12$.

The most striking aspect of the findings displayed in Fig. 5, especially when viewed in conjunction with Fig. 6, is the widely varying characteristics observed between the four cases. For the Volterra and differentiation kernels, at least within the subbasis used here, the number of channels considered has a remarkable influence on the observed limit values. Given that analogous trends are seen in performance of the associated structural optimizations, it can be safely concluded that this behavior is fundamental, hinting that there is a sort of Fourier (resolution) limit at play (e.g., size-dependent constraints on space-bandwidth products are known to limit the degree to which a given optical feature may be resolved with a finite device [89, 90]). Moreover, presumably because dif-

ferentiation demands creation of more rapid profile variations whereas Volterra operations demand only smoothing, loss function values (for both bounds and inverse design) differ by multiple orders of magnitude for small numbers of channels (≈ 3) before reaching "asymptotes" that differ roughly by a factor of 10, for $\chi = 10.7 + i\ 0.01$. Conversely, in the focusing example examined in Fig. 6, the bounds exhibit only a weak dependence on the number of channels in either representative material. While a precise account of the factors leading to these differences is likely challenging, it should be noted that in all cases the objective is bounded (from above or below) by performance that could be achieved in vacuum or a full slab, and so the appearance of plateaus when performance is poor should come as no surprise. A related, albeit more intuitive, dichotomy is seen with respect to the number of clusters imposed and the magnitude of electric susceptibility ($\mathrm{Re}\,[\chi]$). For $\mathrm{Re}\,[\chi] = 2$, subdividing the domain generally leads to substantial tightening, while for $\mathrm{Re}\,[\chi] = 10$ many more clusters are needed to produce meaningful alterations owing to the decrease in the effective wavelength in the medium.

D. Near-field lens (metaoptics)

Objective—Working within a given bounding rectangular design domain, maximize the average field intensity within a specified focal region for a predefined set of incident plane waves spanning a cone of incidence.

The size of the rectangular design region is characterized by the lengths $L_1^d = 0.5\ \lambda$ and $L_2^d = 2\ \lambda$, inset Fig. 6. The focal region is a square centered along L_2^d, with side length $L_1^f = L_2^f = 0.25\ \lambda$. The middle of the focal region is set to reside at a distance of $0.5\ \lambda$ from the outgoing edge of design region. The design objective is

$$\mathrm{Obj}\left(\left\{\left|\mathbf{E}_k^t\right\rangle\right\}\right) = \max \sum_{i=1}^{N} \left\langle \mathbf{E}_i^t \right| \mathbb{I}_{\mathrm{focal}} \left| \mathbf{E}_i^t \right\rangle \qquad (22)$$

where the summation index runs over the N angles of incidence, evenly distributed over a cone of $(N-1)\times 15°$ degrees centered on the midpoint of L_d^2. As before, the cluster labels given in Fig. 6 reference even divisions of the rectangular design domain along its short and long edges: $16 = 2\times 8$, $32 = 4\times 8$, $36 = 3\times 12$, $100 = 5\times 20$, and $256 = 8\times 32$.

Even in comparison to previous examples, the extent to which inverse design is able to approach the limit values produced by the formulation of Sec. II is notable. For a single source (a normally incident planewave), agreement within a factor of 3 is achieved when a single cluster constraint is supposed, and as increasingly localized domain constraints are imposed the performance gap is seen to nearly close. Hence, somewhat surprisingly, the relatively poor field localization values achieved by the topology optimized (inverse design) geometries are in fact not far from ideal. We suspect that three underlying factors are

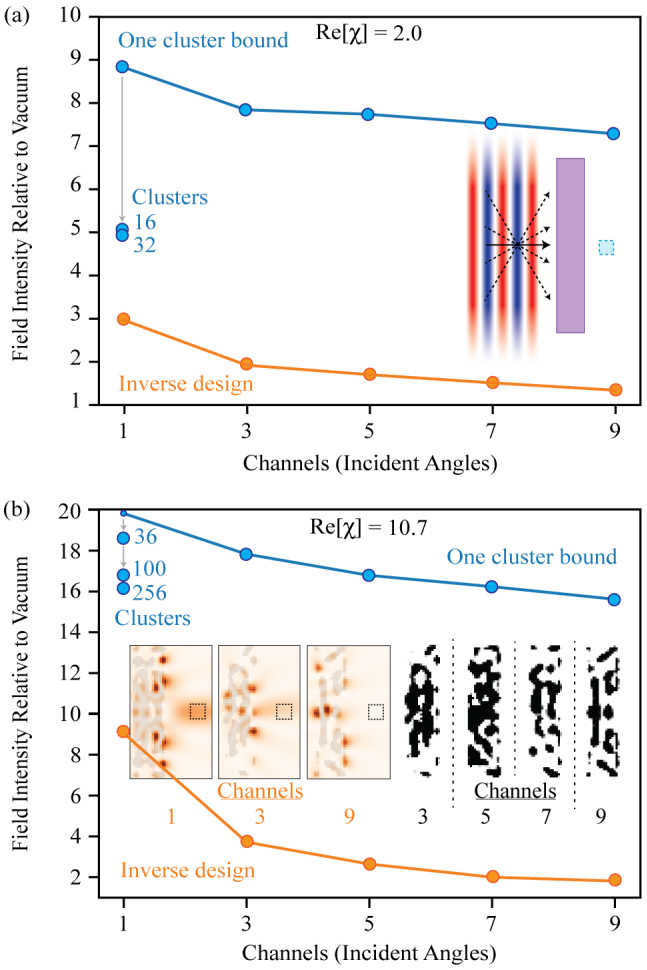

FIG. 6. **Focusing metalens.** Highlighting the applicability of the proposed method to establish limits on metaoptical elements, the figure provides bounds on the ability of any structure confined within a rectangular domain of subwavelength thickness to enhance the average field intensity over a predefined focal region in the near field of the structure, for a given collection of incident planewaves. Also shown are comparative performances of inverse designed structures. A material loss value of $\mathrm{Im}\,[\chi] = 0.01$ is supposed in all cases. Binarized structures for 3, 5, 7 and 9 channels, producing relative field-enhancement factors of 5.27, 2.66, 2.56 and 1.64 respectively, are included as insets. Quoted values for the inverse design curve correspond to "grayscale" structures.

largely responsible for these findings. First, the focusing problem does not impose any specific target profile for the output fields, inset Fig. 6(b), leading to a greater variety of geometric possibilities with similar focusing performance. Second, given the assumed design domain, the specified location and volume of the focal region makes the problem more difficult than what might be naively expected [91]; quite different results may be encountered if the "spot size", or separation between the focus and design domain, are reduced. Third, the extended nature of planewave sources naturally suggests the uniform clus-

ter constraints that have been employed. Contrastingly, for the Volterra and difference kernels, it is plausible that non-uniform cluster distributions, or simply smaller clusters, could lead to tighter bounds. A systematic study of such questions, once a more resource-effective approach for solving Eq. (9) is found [53], remains as an important direction for future work.

IV. SUMMARY DISCUSSION

In summary, we have shown that recently developed methods for calculating limits on sesquilinear electromagnetic objectives [42, 45, 51–53], can be applied to a wide variety of design problems, including spatial multiplexing [22–24], metaoptics [92–95], linear computation [25–27] and light extraction [96–99]. Employing the language of communication theory, this program stands as a significant extension of prior work on channel-based electromagnetic limits [8, 30, 55–60]. Namely, although highly insightful, the characteristics of the background Green's function connecting the volumes containing particular sender and receiver registers are generally insufficient for accurately assessing whether the extent to which some desired communication can occur, particularly in wavelength-scale devices. Rather, as may be confirmed by a survey of the results presented in Sec. III, the degree to which communication between a predefined collection of registers can occur may depend strongly on a range of other environmental factors, such as the physical size and response parameters available for designing the channels, and the spatial profile of the register fields.

The strong correspondence observed between bounds computed with this approach and the findings of inverse design exemplified in Sec. III continues many of the trends seen in the earlier works cited above. Regardless of the particular objective and distribution of cluster constraints considered, we have yet to encounter a situation in which strong duality does not hold [100]. As such, it would seem that the outstanding difficulties of constructing a general toolbox for realizing (tight) limits that incorporate the full wave physics and limitations of Maxwell's equations, and in turn offer guidance for practical designs, are computational [29, 45, 53]. All present evidence indicates that optimization problems following the form of Eq. (15) can be solved exactly via the duality relaxation described in Sec. II. If this is indeed the case, then the matter of central importance is not whether there is some configuration of clusters that will capture all key effects that physically limit communication, but whether some reasonably good approximation can actually be solved in an acceptable amount of time. With this in mind, we believe that the results presented above provide substantial reason for optimism.

Finally, the specificity of the program presented in the main text raises a prescient question pertaining to realizing abstract transformations. Expressly, there are many instances in which the primary concern is how well the transformation can be implemented between a given number of *undetermined* inputs and outputs (channels). The distinction amounts, in essence, to the same shift in perspective advocated for in recent "end-to-end" inverse design formulations [95, 101] and waveform optimization investigations [102, 103]: the exact characteristics of the domain and codomain sets for some particular discrimination or transformation are often mutable, and only important in so far as they implicitly alter achievable performance. The duality program outlined above can be extended to treat this problem in a variety of ways, and we intended to present this analysis in detail in an upcoming work.

ACKNOWLEDGMENTS

This work was supported by the National Science Foundation under the Emerging Frontiers in Research and Innovation (EFRI) program, EFMA-1640986, the Cornell Center for Materials Research (MRSEC) through award DMR-1719875, and the Defense Advanced Research Projects Agency (DARPA) under agreements HR00112090011, HR00111820046 and HR0011047197. The views, opinions and findings expressed herein are those of the authors and should not be interpreted as representing official views or policies of any institution.

V. APPENDIX

A. Off-origin dipole spherical wave expansions

Following results of Ref. [104], as explained in Refs. [64, 105], off-origin, on-axis, outgoing spherical waves can be expanded in terms of on-origin outgoing and regular spherical waves as

$$\mathbf{W}^{\text{out}}_{plm}(\mathbf{r}) = \begin{cases} \sum\limits_{p',l'} \mathcal{U}^{\text{in}\pm}_{p'p,l'lm}(d)\ \mathbf{W}^{\text{reg}}_{p'l'm}(\mathbf{r} \pm d\hat{\mathbf{z}}) & r < d \\ \sum\limits_{p',l'} \mathcal{U}^{\text{out}\pm}_{p'p,l'lm}(d)\ \mathbf{W}^{\text{out}}_{p'l'm}(\mathbf{r} \pm d\hat{\mathbf{z}}) & r > d \end{cases}, \tag{23}$$

where

$$\mathcal{U}^{\text{in}\pm}_{p'p,l'lm}(d) = \sum_{\nu}\left[\frac{l(l+1)+l'(l'+1)-\nu(\nu+1)}{2}\delta_{pp'} \mp i\ mdk_o(1-\delta_{pp'})\right]A^{h\pm}_{l'l\nu m}(d), \tag{24}$$

$$\mathcal{U}^{\text{out}\pm}_{p'p,l'lm}(d) = \sum_{\nu}\left[\frac{l(l+1)+l'(l'+1)-\nu(\nu+1)}{2}\delta_{pp'} \mp i\ mdk_o(1-\delta_{pp'})\right]A^{j\pm}_{l'l\nu m}(d), \tag{25}$$

$$A^{h\pm}_{l'l\nu m}(d) = (-1)^m i^{l-l'\pm\nu}(2\nu+1)\sqrt{\frac{(2l+1)(2l'+1)}{l(l+1)l'(l'+1)}}\begin{pmatrix} l & l' & \nu \\ 0 & 0 & 0\end{pmatrix}\begin{pmatrix} l & l' & \nu \\ m & -m & 0\end{pmatrix} h_\nu(dk_o), \tag{26}$$

$$A^{j\pm}_{l'l\nu m}(d) = (-1)^m i^{l-l'\pm\nu}(2\nu+1)\sqrt{\frac{(2l+1)(2l'+1)}{l(l+1)l'(l'+1)}}\begin{pmatrix} l & l' & \nu \\ 0 & 0 & 0\end{pmatrix}\begin{pmatrix} l & l' & \nu \\ m & -m & 0\end{pmatrix} j_\nu(dk_o). \tag{27}$$

In Eqs. (24)–(27), the large round brackets are Wigner-3j symbols, j_ν and h_ν denote the spherical Bessel and Hankel functions of the first kind respectively, and the plus and minus signs indicate the sign of the necessary coordinate transformation. Noting that the field of a $\hat{\mathbf{z}}$-polarized dipole radiation consists entirely of the $\mathbf{N}_{1,0}$ outgoing wave,

$$\mathbf{E}^z(r,\theta,\phi) = \frac{ik_o}{\sqrt{6\pi}}\mathbf{N}_{1,0}(r,\theta,\phi), \tag{28}$$

the field of an off-axis dipole can thus be computed from Eqs. (24)–(27) by setting $p = N$, $l = 1$, and $m = 0$ implying, through the Wigner selection rules that the on-origin regular M waves, Rg$\mathbf{M}$, waves need not be included. Using this knowledge, the expansion coefficients for an off-origin, on-axis, dipole can be reduce to

$$\begin{aligned}\mathbf{E}^z_{-d\hat{\mathbf{z}}}(\mathbf{r}) &= \frac{ik_o}{\sqrt{6\pi}}\mathbf{N}_{1,0}(\mathbf{r}+d\hat{\mathbf{z}}) \\ &= \begin{cases}\frac{ik_o}{\sqrt{6\pi}}\sum_{l=1}^{\infty}\mathcal{U}^{\text{in}-}_{NN,l,1,0}\text{Rg}\mathbf{N}_{l,0}(\mathbf{r}) & (r<d), \\ \frac{ik_o}{\sqrt{6\pi}}\sum_{l=1}^{\infty}\mathcal{U}^{\text{out}-}_{NN,l,1,0}\mathbf{N}_{l,0}(\mathbf{r}) & (r>d),\end{cases}\end{aligned} \tag{29}$$

$$\begin{aligned}\mathbf{E}^z_{+d\hat{\mathbf{z}}}(\mathbf{r}) &= \frac{ik_o}{\sqrt{6\pi}}\mathbf{N}_{1,0}(\mathbf{r}-d\hat{\mathbf{z}}) \\ &= \begin{cases}\frac{ik_o}{\sqrt{6\pi}}\sum_{l=1}^{\infty}\mathcal{U}^{\text{in}+}_{NN,l,1,0}\text{Rg}\mathbf{N}_{l,0}(\mathbf{r}) & (r<d), \\ \frac{ik_o}{\sqrt{6\pi}}\sum_{l=1}^{\infty}\mathcal{U}^{\text{out}+}_{NN,l,1,0}\mathbf{N}_{l,0}(\mathbf{r}) & (r>d),\end{cases}\end{aligned} \tag{30}$$

where

$$\mathcal{U}^{\text{in}-}_{NN,l,1,0} = \sum_{\nu=l-1}^{l+1} L^\nu_l \begin{pmatrix} 1 & l & \nu \\ 0 & 0 & 0\end{pmatrix}^2 h_\nu(dk_o), \tag{31}$$

$$\mathcal{U}^{\text{in}+}_{NN,l,1,0} = \sum_{\nu=l-1}^{l+1} (-1)^\nu L^\nu_l \begin{pmatrix} 1 & l & \nu \\ 0 & 0 & 0\end{pmatrix}^2 h_\nu(dk_o). \tag{32}$$

$\mathcal{U}^{\text{out}-}_{NN,l,1,0}$ and $\mathcal{U}^{\text{out}+}_{NN,l,1,0}$ are equivalently defined but with the Hankel functions of the first kind, $h_\nu(dk_o)$, replaced by Bessel functions of the first kind. In these expressions, summation limits are set by explicit evaluation of the Wigner-3j selection rules and

$$L^\nu_l = (2\nu+1)\frac{2+l(l+1)-\nu(\nu+1)}{2}i^{1-\nu-l}\sqrt{\frac{6l+3}{2l(l+1)}}. \tag{33}$$

B. Computation for two-dimensional examples

The Green's function representations used for computing bounds in all two-dimensional examples were obtained by the open-source *ceviche* FDFD package [106]. The basis used for representing fields in all such cases are the individual discretization pixels of the FDFD computation. Correspondingly, the matrix representation of the Green's function connects every pixel with a numeric approximation of the field generated by a dipole source at the location of the pixel.

For all studies with a free space background, the translational invariance of the Maxwell is exploited to construct the matrix representation of the Green's function from a single dipole field solve. Concretely, consider a domain of shape (N_x, N_y) in pixels. The required representation of $\mathbb{G}^0$ is then a square matrix of dimension N_xN_y, where the j-th column is the field created by an electric dipole at position j. This matrix can be obtained in a single solve by placing a dipole at the center of a larger $(2N_x-1, 2N_y-1)$ domain and observing the calculated field in sliding a window of size (N_x, N_y).

To account for the cross-source constraints in the presence of multiple sources, compared to the approaches we have used in prior works [45], the fields and matrices for each of the individual sources are grouped into "super" vectors and matrices:

$$|\mathbf{T}\rangle = \begin{bmatrix}|\mathbf{T}_1\rangle \\ \vdots \\ |\mathbf{T}_N\rangle\end{bmatrix} \quad \mathbb{Z}^{TT} = \begin{bmatrix}\mathbb{Z}^{T_1T_1} & \dots & \mathbb{Z}^{T_1T_N} \\ \vdots & \ddots & \vdots \\ \mathbb{Z}^{T_NT_1} & \dots & \mathbb{Z}^{T_NT_N}\end{bmatrix} \tag{34}$$

As such, the dimension of the vectors and matrices involved in the calculation of a N-source bound scales linearly with N. To facilitate computation of bounds for

large device footprints and values of N, an Arnoldi basis for $\mathbb{U}$ is computed to more efficiently represent the $|\mathbf{T}\rangle$ image field. For any given problem, the only vectors that interact with the primal degrees of freedom, $\{|\mathbf{T}_n\rangle\}$, are the sources, $\{|\mathbf{E}_n^i\rangle\}$, and the linear coefficients of $\{|\mathbf{T}_n\rangle\}$ in the primal objective $\{|\mathcal{O}_n^{\text{lin}}\rangle\}$. Hence, these vectors

$$B_0 = \left[|\mathbf{E}_1^i\rangle \ \ldots \ |\mathbf{E}_N^i\rangle \ |\mathcal{O}_1^{\text{lin}}\rangle \ \ldots \ |\mathcal{O}_1^{\text{lin}}\rangle\right], \tag{35}$$

posses favorable convergence characteristic for computing the dual via Arnoldi iterations. For communications type problems $|\mathcal{O}_n^{\text{lin}}\rangle = \mathbb{G}_{od}^{\dagger}\left(|\mathbf{E}_n^{\diamond}\rangle - |\mathbf{E}_n^i\rangle\right)$, while for the metalens problem $|\mathcal{O}_n^{\text{lin}}\rangle = \mathbb{G}_{od}^{\dagger}|\mathbf{E}_n^i\rangle$. To begin the Arnoldi procedure, B_0 is orthonormalized to give $\bar{B}_0$. The i-th iteration is then computed by generating $B_i = \mathbb{U}\bar{B}_{i-1}$, and then orthonormalizing B_i both internally and with respect to $\bar{B}_0, \ldots, \bar{B}_{i-1}$, giving $\bar{B}_i$. The partial basis for the generated block Krylov subspace at the end of the i-th iteration is the thus the aggregate of all the column vectors of $\bar{B}_0, \ldots, \bar{B}_i$. Denoting $\mathbb{U}$ restricted to the i-th Krylov subspace as $\mathbb{U}_i$, the representation is effectively complete when the column norms of $\mathbb{U}_i^{-1}\bar{B}_0$ converge to within a certain tolerance, Ref. [29].

Inverse design results for all two dimensional examples are also computed using *ceviche* using a standard topology optimization [91]. For sake of comparison with the optimization problem underlying the bound formulation, grayscale structures are treated as viable. That is, in any particular design, the permittivity value of a given pixel can take any value in the convex set bounded by 0 and the quoted material value.

[1] Sergio Verdu. Fifty years of Shannon theory. *IEEE Transactions on information theory*, 44(6):2057–2078, 1998.

[2] Pierre-Marie Robitaille. Kirchhoff's law of thermal emission: 150 years. *Progress in Physics*, 4:3–13, 2009.

[3] Claude E Shannon. A mathematical theory of communication. *The Bell System Technical Journal*, 27(3): 379–423, 1948.

[4] John Brian Pendry. Quantum limits to the flow of information and entropy. *Journal of Physics A: Mathematical and General*, 16(10):2161, 1983.

[5] Carlton M Caves and Peter D Drummond. Quantum limits on bosonic communication rates. *Reviews of Modern Physics*, 66(2):481, 1994.

[6] Michał Horodecki, Paweł Horodecki, and Ryszard Horodecki. Limits for entanglement measures. *Physical Review Letters*, 84(9):2014, 2000.

[7] Stefano Pirandola, Riccardo Laurenza, Carlo Ottaviani, and Leonardo Banchi. Fundamental limits of repeaterless quantum communications. *Nature communications*, 8(1):1–15, 2017.

[8] David AB Miller. Waves, modes, communications, and optics: a tutorial. *Advances in Optics and Photonics*, 11(3):679–825, 2019.

[9] Eli Yablonovitch. Statistical ray optics. *Journal of the Optical Society of America*, 72(7):899–907, 1982.

[10] Dennis M Callahan, Jeremy N Munday, and Harry A Atwater. Solar cell light trapping beyond the ray optic limit. *Nano letters*, 12(1):214–218, 2012.

[11] Andrey E Miroshnichenko and Michael I Tribelsky. Ultimate absorption in light scattering by a finite obstacle. *Physical Review Letters*, 120(3):033902, 2018.

[12] Hila Hashemi, Baile Zhang, John D Joannopoulos, and Steven G Johnson. Delay-bandwidth and delay-loss limitations for cloaking of large objects. *Physical Review Letters*, 104(25):253903, 2010.

[13] Francesco Monticone and Andrea Alù. Invisibility exposed: physical bounds on passive cloaking. *Optica*, 3 (7):718–724, 2016.

[14] Maxence Cassier and Graeme W Milton. Bounds on herglotz functions and fundamental limits of broadband passive quasistatic cloaking. *Journal of Mathematical Physics*, 58(7):071504, 2017.

[15] H. John Caulfield and Tomas Hirschfeld. Optical communication at the source bandwidth limit. *Applied Optics*, 16(5):1184–1186, 1977.

[16] Kosmas L Tsakmakidis, Linfang Shen, Sebastian A Schulz, Xiaodong Zheng, John Upham, Xiaohua Deng, Hatice Altug, Alexander F Vakakis, and Robert W Boyd. Breaking lorentz reciprocity to overcome the time-bandwidth limit in physics and engineering. *Science*, 356(6344):1260–1264, 2017.

[17] Sander A Mann, Dimitrios L Sounas, and Andrea Alù. Nonreciprocal cavities and the time–bandwidth limit. *Optica*, 6(1):104–110, 2019.

[18] Yaser S Abu-Mostafa and Demetri Psaltis. Optical neural computers. *Scientific American*, 256(3):88–95, 1987.

[19] Tyler W Hughes, Ian AD Williamson, Momchil Minkov, and Shanhui Fan. Wave physics as an analog recurrent neural network. *Science advances*, 5(12):eaay6946, 2019.

[20] Ying Zuo, Bohan Li, Yujun Zhao, Yue Jiang, You-Chiuan Chen, Peng Chen, Gyu-Boong Jo, Junwei Liu, and Shengwang Du. All-optical neural network with nonlinear activation functions. *Optica*, 6(9):1132–1137, 2019.

[21] Wim Bogaerts, Daniel Pérez, José Capmany, David AB Miller, Joyce Poon, Dirk Englund, Francesco Morichetti, and Andrea Melloni. Programmable photonic circuits. *Nature*, 586(7828):207–216, 2020.

[22] David J Richardson, John M Fini, and Lynn E Nelson. Space-division multiplexing in optical fibres. *Nature Photonics*, 7(5):354–362, 2013.

[23] Juhao Li, Fang Ren, Tao Hu, Zhengbin Li, Yongqi He, Zhangyuan Chen, Qi Mo, and Guifang Li. Recent progress in mode-division multiplexed passive optical networks with low modal crosstalk. *Optical Fiber Technology*, 35:28–36, 2017.

[24] Zhenshan Yang, Xiaoguang Zhang, Bin Zhang, Xia Zhang, Zhentao Zhang, Xiangguo Meng, and Chenglin Bai. Density-matrix formalism for modal coupling and dispersion in mode-division multiplexing communications systems. *Optics Express*, 28(13):18658–18680,

2020.

[25] Nasim Mohammadi Estakhri, Brian Edwards, and Nader Engheta. Inverse-designed metastructures that solve equations. *Science*, 363(6433):1333–1338, 2019.

[26] Lianlin Li, Ya Shuang, Qian Ma, Haoyang Li, Hanting Zhao, Menglin Wei, Che Liu, Chenglong Hao, Cheng-Wei Qiu, and Tie Jun Cui. Intelligent metasurface imager and recognizer. *Light: Science & Applications*, 8 (1):1–9, 2019.

[27] Hamid Rajabalipanah, Ali Abdolali, Shahid Iqbal, Lei Zhang, and Tie Jun Cui. How do space-time digital metasurfaces serve to perform analog signal processing? *arXiv:2002.06773*, 2020.

[28] Vittorio Giovannetti, Seth Lloyd, Lorenzo Maccone, and Jeffrey H Shapiro. Sub-rayleigh-diffraction-bound quantum imaging. *Physical Review A*, 79(1):013827, 2009.

[29] Sean Molesky, Pengning Chao, Weiliang Jin, and Alejandro W Rodriguez. Global $\mathbb{T}$-operator bounds on electromagnetic scattering: Upper bounds on far-field cross sections. *Physical Review Research*, 2(3):033172, 2020.

[30] Owen D Miller, Steven G Johnson, and Alejandro W Rodriguez. Shape-independent limits to near-field radiative heat transfer. *Physical Review Letters*, 115(20): 204302, 2015.

[31] Weiliang Jin, Sean Molesky, Zin Lin, and Alejandro W Rodriguez. Material scaling and frequency-selective enhancement of near-field radiative heat transfer for lossy metals in two dimensions via inverse design. *Physical Review B*, 99(4):041403(R), 2019.

[32] Prashanth S Venkataram, Sean Molesky, Weiliang Jin, and Alejandro W Rodriguez. Fundamental limits to radiative heat transfer: the limited role of nanostructuring in the near-field. *Physical Review Letters*, 124(1): 013904, 2020.

[33] Alexander Y Piggott, Jesse Lu, Thomas M Babinec, Konstantinos G Lagoudakis, Jan Petykiewicz, and Jelena Vučković. Inverse design and implementation of a wavelength demultiplexing grating coupler. *Scientific Reports*, 4(1):1–5, 2014.

[34] Andrew Michaels and Eli Yablonovitch. Inverse design of near unity efficiency perfectly vertical grating couplers. *Optics express*, 26(4):4766–4779, 2018.

[35] Jianji Yang, David Sell, and Jonathan A Fan. Freeform metagratings based on complex light scattering dynamics for extreme, high efficiency beam steering. *Annalen der Physik*, 530(1):1700302, 2018.

[36] Prachi Thureja, Ghazaleh Kafaie Shirmanesh, Katherine T Fountaine, Ruzan Sokhoyan, Meir Grajower, and Harry A Atwater. Array-level inverse design of beam steering active metasurfaces. *ACS Nano*, 2020.

[37] Oguzhan Akgol, Emin Unal, Olcay Altintas, Muharrem Karaaslan, Faruk Karadag, and Cumali Sabah. Design of metasurface polarization converter from linearly polarized signal to circularly polarized signal. *Optik*, 161: 12–19, 2018.

[38] Haejun Chung and Owen D Miller. High-na achromatic metalenses by inverse design. *Optics Express*, 28(5): 6945–6965, 2020.

[39] Jesse Lu and Jelena Vučković. Inverse design of nanophotonic structures using complementary convex optimization. *Optics Express*, 18(4):3793–3804, 2010.

[40] Jesse Lu and Jelena Vučković. Objective-first design of high-efficiency, small-footprint couplers between arbitrary nanophotonic waveguide modes. *Optics express*, 20(7):7221–7236, 2012.

[41] Owen D Miller, Athanasios G Polimeridis, M. T. Homer Reid, Chia Wei Hsu, Brendan G DeLacy, John D Joannopoulos, Marin Soljačić, and Steven G Johnson. Fundamental limits to optical response in absorptive systems. *Optics Express*, 24(4):3329–3364, 2016.

[42] Guillermo Angeris, Jelena Vučković, and Stephen P Boyd. Computational bounds for photonic design. *ACS Photonics*, 6(5):1232, 2019. doi: 10.1021/acsphotonics.9b00154.

[43] Sean Molesky, Weiliang Jin, Prashanth S Venkataram, and Alejandro W Rodriguez. $\mathbb{T}$-operator bounds on angle-integrated absorption and thermal radiation for arbitrary objects. *Physical Review Letters*, 123:257401, 2019.

[44] Sean Molesky, Prashanth S Venkataram, Weiliang Jin, and Alejandro W Rodriguez. Fundamental limits to radiative heat transfer: theory. *Physical Review B*, 101 (3):035408, 2020.

[45] Sean Molesky, Pengning Chao, and Alejandro W Rodriguez. Hierarchical mean-field $\mathbb{T}$-operator bounds on electromagnetic scattering: Upper bounds on near-field radiative purcell enhancement. *Physical Review Research*, 2(4):043398, 2020.

[46] Mats Gustafsson, Kurt Schab, Lukas Jelinek, and Miloslav Capek. Upper bounds on absorption and scattering. *New Journal of Physics*, 2020.

[47] Prashanth S Venkataram, Sean Molesky, Pengning Chao, and Alejandro W Rodriguez. Fundamental limits to attractive and repulsive casimir-polder forces. *Physical Review A*, 101(5):052115, 2020.

[48] Zeyu Kuang, Lang Zhang, and Owen D Miller. Maximal single-frequency electromagnetic response. *arXiv:2002.00521*, 2020.

[49] Kurt Schab, Austin Rothschild, Kristi Nguyen, Miloslav Capek, Lukas Jelinek, and Mats Gustafsson. Tradeoffs in absorption and scattering by nanophotonic structures. *Optics Express*, 28(24):36584–36599, 2020.

[50] Rahul Trivedi, Guillermo Angeris, Logan Su, Stephen Boyd, Shanhui Fan, and Jelena Vuckovic. Fundamental bounds for scattering from absorptionless electromagnetic structures. *arXiv:2003.00374*, 2020.

[51] Zeyu Kuang and Owen D Miller. Computational bounds to light-matter interactions via local conservation laws. *arXiv preprint arXiv:2008.13325*, 2020.

[52] L Jelinek, M Gustafsson, M Capek, and K Schab. Substructure limits to optical phenomena. In *2020 Fourteenth International Congress on Artificial Materials for Novel Wave Phenomena (Metamaterials)*, pages 400–402. IEEE.

[53] Guillermo Angeris, Jelena Vučković, and Stephen Boyd. Heuristic methods and performance bounds for photonic design. *Optics Express*, 29(2):2827–2854, 2021.

[54] Walter Rudin. *Real and complex analysis*. Tata McGraw-hill education, 2006.

[55] David AB Miller. All linear optical devices are mode converters. *Optics express*, 20(21):23985–23993, 2012.

[56] David AB Miller. Self-configuring universal linear optical component. *Photonics Research*, 1(1):1–15, 2013.

[57] David AB Miller, Linxiao Zhu, and Shanhui Fan. Universal modal radiation laws for all thermal emitters. *Proceedings of the National Academy of Sciences*, 114 (17):4336–4341, 2017.

[58] Sunil Pai, Ben Bartlett, Olav Solgaard, and David AB Miller. Matrix optimization on universal unitary photonic devices. *Physical Review Applied*, 11(6):064044, 2019.

[59] David A B Miller. Fundamental limit for optical components. *Journal of the Optical Society of America B*, 24(10):A1–A18, 2007.

[60] David AB Miller. How complicated must an optical component be? *JOSA A*, 30(2):238–251, 2013.

[61] Leung Tsang, Jin Au Kong, and Kung-Hau Ding. *Scattering of electromagnetic waves: Theories and applications*, volume 27. John Wiley & Sons, 2004.

[62] Andreas Kirsch and Armin Lechleiter. The operator equations of Lippmann–Schwinger type for acoustic and electromagnetic scattering problems in L2. *Applicable Analysis*, 88(6):807–830, 2009.

[63] Martin Costabel, Eric Darrigrand, and Hamdi Sakly. The essential spectrum of the volume integral operator in electromagnetic scattering by a homogeneous body. 2012.

[64] Matthias Krüger, Giuseppe Bimonte, Thorsten Emig, and Mehran Kardar. Trace formulas for nonequilibrium casimir interactions, heat radiation, and heat transfer for arbitrary objects. *Physical Review B*, 86(11):115423, 2012.

[65] David Colton and Rainer Kress. *Inverse acoustic and electromagnetic scattering theory*, volume 93. Springer Nature, 2019.

[66] Note1. All operators and fields are supposed to be frequency dependent, and every stated relation holds at any given frequency.

[67] Note2. The potential of the scatterer is constructed via the explicit spatial projection operator $\mathbb{I}_s$, which is defined to be identity at spatial locations within the scatterer and zero at all other points in the domain Ω, and the implicit spatial projection into the scattering object encoded in the definition the scattering operator, $\mathbb{T}_s$.

[68] Note3. The specification of an initial field is essentially equivalent to the introduction of a source, or flux boundary condition, in Maxwell's equations.

[69] Jingfeng Liu, Ming Zhou, Lei Ying, Xuewen Chen, and Zongfu Yu. Enhancing the optical cross section of quantum antenna. *Physical Review A*, 95(1):013814, 2017.

[70] A Femius Koenderink. Single-photon nanoantennas. *ACS Photonics*, 4(4):710–722, 2017.

[71] Kevin C Cox, David H Meyer, Fredrik K Fatemi, and Paul D Kunz. Quantum-limited atomic receiver in the electrically small regime. *Physical Review Letters*, 121 (11):110502, 2018.

[72] Sudha Mokkapati and KR Catchpole. Nanophotonic light trapping in solar cells. *Journal of Applied Physics*, 112(10):101101, 2012.

[73] Xing Sheng, Juejun Hu, Jurgen Michel, and Lionel C Kimerling. Light trapping limits in plasmonic solar cells: an analytical investigation. *Optics Express*, 20 (104):A496–A501, 2012.

[74] Vidya Ganapati, Owen D Miller, and Eli Yablonovitch. Light trapping textures designed by electromagnetic optimization for subwavelength thick solar cells. *IEEE Journal of Photovoltaics*, 4(1):175–182, 2013.

[75] E Phan-huy Hao. Quadratically constrained quadratic programming: Some applications and a method for solution. *Zeitschrift für Operations Research*, 26(1):105–119, 1982.

[76] Subhonmesh Bose, Dennice F Gayme, K Mani Chandy, and Steven H Low. Quadratically constrained quadratic programs on acyclic graphs with application to power flow. *IEEE Transactions on Control of Network Systems*, 2(3):278–287, 2015.

[77] Note4. Technically, $\mathcal{B}$ should be complete, and hence infinite dimensional. In practice, however, $\mathcal{B}$ must truncated to some finite set in order to apply numerical methods. A similar approximation is needed in any numeric solver for electromagnetics.

[78] Jaehyun Park and Stephen Boyd. General heuristics for nonconvex quadratically constrained quadratic programming. *arXiv:1703.07870*, 2017.

[79] Stephen Boyd and Lieven Vandenberghe. *Convex optimization*. Cambridge university press, 2004.

[80] Note5. Cluster refinements, as shown in Ref. [45], can be given a mathematical ordering that is preserved in the limit values obtained in the associated optimization, whether or not the dual is used to relax the optimization.

[81] Note6. In particular, if $\Omega_c = \Omega$, so that there is only a single cluster filling the entire domain, then the symmetric ($\mathrm{Sym}\left[\mathbb{A}\right] = \left(\mathbb{A} + \mathbb{A}^\dagger\right)/2$) and antisymmetric ($\mathrm{Sym}\left[\mathbb{A}\right] = \left(\mathbb{A} + \mathbb{A}^\dagger\right)/2$) parts of the scattering constraints impose that both real and reactive power must be conserved, as was studied in Refs. [43, 46].

[82] Timm Plefka. Convergence condition of the tap equation for the infinite-ranged ising spin glass model. *Journal of Physics A*, 15(6):1971, 1982.

[83] Jiasen Jin, Alberto Biella, Oscar Viyuela, Leonardo Mazza, Jonathan Keeling, Rosario Fazio, and Davide Rossini. Cluster mean-field approach to the steady-state phase diagram of dissipative spin systems. *Physical Review X*, 6(3):031011, 2016.

[84] Mojtaba Nourian and Peter E Caines. ϵ-nash mean field game theory for nonlinear stochastic dynamical systems with major and minor agents. *SIAM Journal on Control and Optimization*, 51(4):3302–3331, 2013.

[85] Nevroz Şen and Peter E Caines. Mean field game theory with a partially observed major agent. *SIAM Journal on Control and Optimization*, 54(6):3174–3224, 2016.

[86] Hilbert J Kappen and Francisco de Borja Rodríguez Ortiz. Boltzmann machine learning using mean field theory and linear response correction. In *Advances in Neural Information Processing Systems*, pages 280–286, 1998.

[87] Minmin Chen, Jeffrey Pennington, and Samuel S Schoenholz. Dynamical isometry and a mean field theory of rnns: Gating enables signal propagation in recurrent neural networks. *arXiv:1806.05394*, 2018.

[88] Note7. Duality can also be used to solve a relaxation of the mean-field optimization that in many cases is in fact a true solution [79].

[89] David Mendlovic and Adolf W Lohmann. Space–bandwidth product adaptation and its application to superresolution: fundamentals. *JOSA A*, 14(3):558–562, 1997.

[90] Mark A Neifeld. Information, resolution, and space–bandwidth product. *Optics Letters*, 23(18):1477–1479, 1998.

[91] Rasmus E Christiansen and Ole Sigmund. Inverse design in photonics by topology optimization: tutorial. *JOSA B*, 38(2):496–509, 2021.

[92] Sergey Kruk and Yuri Kivshar. Functional meta-optics and nanophotonics governed by mie resonances. *ACS Photonics*, 4(11):2638–2649, 2017.

[93] Tomer Lewi, Nikita A Butakov, Hayden A Evans, Mark W Knight, Prasad P Iyer, David Higgs, Hamid Chorsi, Juan Trastoy, Javier Del Valle Granda, Ilya Valmianski, et al. Thermally reconfigurable meta-optics. *IEEE Photonics Journal*, 11(2):1–16, 2019.

[94] Isabelle Staude, Thomas Pertsch, and Yuri S Kivshar. All-dielectric resonant meta-optics lightens up. *ACS Photonics*, 6(4):802–814, 2019.

[95] Zin Lin, Charles Roques-Carmes, Raphaël Pestourie, Marin Soljačić, Arka Majumdar, and Steven G Johnson. End-to-end inverse design for inverse scattering via freeform metastructures. *arXiv:2006.09145*, 2020.

[96] Philipp-Immanuel Schneider, Nicole Srocka, Sven Rodt, Lin Zschiedrich, Stephan Reitzenstein, and Sven Burger. Numerical optimization of the extraction efficiency of a quantum-dot based single-photon emitter into a single-mode fiber. *Optics Express*, 26(7):8479–8492, 2018.

[97] Lian Shen, Xiao Lin, Mikhail Y Shalaginov, Tony Low, Xianmin Zhang, Baile Zhang, and Hongsheng Chen. Broadband enhancement of on-chip single-photon extraction via tilted hyperbolic metamaterials. *Applied Physics Reviews*, 7(2):021403, 2020.

[98] Raymond A Wambold, Zhaoning Yu, Yuzhe Xiao, Benjamin Bachman, Gabriel Jaffe, Shimon Kolkowitz, Jennifer T Choy, Mark A Eriksson, Robert J Hamers, and Mikhail A Kats. Adjoint-optimized nanoscale light extractor for nitrogen-vacancy centers in diamond. *Nanophotonics*, 10(1):393–401, 2021.

[99] Srivatsa Chakravarthi, Pengning Chao, Christian Pederson, Sean Molesky, Karine Hestroffer, Fariba Hatami, Alejandro W Rodriguez, and Kai-Mei C Fu. Inverse-designed photon extractors for optically addressable defect qubits. *arXiv:2007.12344*, 2020.

[100] Note8. It should be mentioned that we have encountered situations in which very high numeric precision was required to verify the presence of strong duality.

[101] Jack Valmadre, Luca Bertinetto, Joao Henriques, Andrea Vedaldi, and Philip HS Torr. End-to-end representation learning for correlation filter based tracking. In *Proceedings of the IEEE Conference on Computer Vision and Pattern Recognition*, pages 2805–2813, 2017.

[102] Lisa A Poyneer and Jean-Pierre Véran. Optimal modal fourier-transform wavefront control. *JOSA A*, 22(8): 1515–1526, 2005.

[103] Vincent Sitzmann, Steven Diamond, Yifan Peng, Xiong Dun, Stephen Boyd, Wolfgang Heidrich, Felix Heide, and Gordon Wetzstein. End-to-end optimization of optics and image processing for achromatic extended depth of field and super-resolution imaging. *ACM Transactions on Graphics (TOG)*, 37(4):1–13, 2018.

[104] Ronald C Wittmann. Spherical wave operators and the translation formulas. *IEEE Transactions on Antennas and Propagation*, 36(8):1078–1087, 1988.

[105] Yu-lin Xu. Calculation of the addition coefficients in electromagnetic multisphere-scattering theory. *Journal of Computational Physics*, 127(2):285–298, 1996.

[106] Tyler W Hughes, Ian AD Williamson, Momchil Minkov, and Shanhui Fan. Forward-mode differentiation of maxwell's equations. *ACS Photonics*, 6(11):3010–3016, 2019.